

AD \_\_\_\_\_

Award Number: W81XWH-11-1-0362

TITLE: Y @ | ^ Á ð Á ^ ç [ | \ • Á | Á | ^ æ ( ^ } o Á - Á ] ð ^ ] • ^

PRINCIPAL INVESTIGATOR: Ken Sakaie, Ph.D.

CONTRACTING ORGANIZATION: The Cleveland Clinic Foundation  
Cleveland, OH 44195-0002

REPORT DATE: July 2013

TYPE OF REPORT: Final

PREPARED FOR: U.S. Army Medical Research and Materiel Command  
Fort Detrick, Maryland 21702-5012

DISTRIBUTION STATEMENT: Approved for Public Release;  
Distribution Unlimited

The views, opinions and/or findings contained in this report are those of the author(s) and should not be construed as an official Department of the Army position, policy or decision unless so designated by other documentation.

REPORT DOCUMENTATION PAGE				Form Approved OMB No. 0704-0188	
Public reporting burden for this collection of information is estimated to average 1 hour per response, including the time for reviewing instructions, searching existing data sources, gathering and maintaining the data needed, and completing and reviewing this collection of information. Send comments regarding this burden estimate or any other aspect of this collection of information, including suggestions for reducing this burden to Department of Defense, Washington Headquarters Services, Directorate for Information Operations and Reports (0704-0188), 1215 Jefferson Davis Highway, Suite 1204, Arlington, VA 22202-4302. Respondents should be aware that notwithstanding any other provision of law, no person shall be subject to any penalty for failing to comply with a collection of information if it does not display a currently valid OMB control number. PLEASE DO NOT RETURN YOUR FORM TO THE ABOVE ADDRESS.					
1. REPORT DATE July 2013		2. REPORT TYPE Final		3. DATES COVERED 1 July 2011 – 30 June 2013	
4. TITLE AND SUBTITLE  Y @   ^ Á ¢ ¢ Á ^ ¢ [ \ • Á {   Á   ^ ¢ ¢ ^ } ¢ Á - Á ¢ ¢ ¢ ] • ^				5a. CONTRACT NUMBER	
				5b. GRANT NUMBER W81XWH-11-1-0362	
				5c. PROGRAM ELEMENT NUMBER	
6. AUTHOR(S)  Ken Sakaie, Ph.D.  E-Mail: sakaiek@ccf.org				5d. PROJECT NUMBER	
				5e. TASK NUMBER	
				5f. WORK UNIT NUMBER	
7. PERFORMING ORGANIZATION NAME(S) AND ADDRESS(ES)  The Cleveland Clinic Foundation Cleveland, OH 44195-0002				8. PERFORMING ORGANIZATION REPORT NUMBER	
9. SPONSORING / MONITORING AGENCY NAME(S) AND ADDRESS(ES) U.S. Army Medical Research and Materiel Command Fort Detrick, Maryland 21702-5012				10. SPONSOR/MONITOR'S ACRONYM(S)	
				11. SPONSOR/MONITOR'S REPORT NUMBER(S)	
12. DISTRIBUTION / AVAILABILITY STATEMENT Approved for Public Release; Distribution Unlimited					
13. SUPPLEMENTARY NOTES					
14. ABSTRACT  The most significant finding during this research period was a clear theoretical foundation for partial differential equation (PDE)-based tractography that inherently includes constraints within the formalism. This foundation has enabled us to make rational choices in developing an algorithm capable of mapping whole-brain networks of axonal connectivity. The algorithm satisfies two necessary conditions: 1) it can identify connections invisible to standard streamline throughout the entire brain and 2) it is fast enough for practical use. Although correlation with gold-standard electrophysiology measurements of connectivity is weak, the developed formalism will make it practical to incorporate information from other imaging modalities with the long range goal of developing a noninvasive biomarker for traumatic brain injury-related epilepsy.					
15. SUBJECT TERMS Traumatic Brain Injury. Epilepsy. Tractography. Electrophysiology. Connectivity.					
16. SECURITY CLASSIFICATION OF:			17. LIMITATION OF ABSTRACT	18. NUMBER OF PAGES	19a. NAME OF RESPONSIBLE PERSON
a. REPORT	b. ABSTRACT	c. THIS PAGE			USAMRMC
U	U	U	UU		19b. TELEPHONE NUMBER (include area code)

## Table of Contents

	<u>Page</u>
Introduction.....	4
Body.....	4
Key Research Accomplishments.....	5
Reportable Outcomes.....	5
Conclusion.....	5
References.....	5
Appendices.....	6

## INTRODUCTION

The primary goal of the 1 year no-cost extension to this grant was to publish results. This goal has been achieved with publication in IEEE Transactions in Medical Imaging (1).

This project addressed the FY10 PRMRP *subject* of epilepsy. Increasing incidence of traumatic brain injury (TBI) among soldiers will likely lead to elevated levels of disability due to TBI-related seizures and epilepsy. The lack of a reliable biomarker hinders efforts to interrupt the evolution of epilepsy from TBI. A new, network paradigm for analysis of brain imaging data suggests a new direction for diagnosing brain injury. Existing analyses have neither been applied to epilepsy nor have been validated by gold standard data. The *purpose* of this research was to initiate exploration of the concept that network properties of imaging data within the *scope* of predicting the transition of TBI to epilepsy. The specific objectives of this project were to develop a fast analysis protocol and validate the analysis with gold-standard invasive electrophysiology measurements from epilepsy patients. The innovative aspects of the research are application of a partial differential equation framework for fast analysis, the application of the network paradigm to epilepsy patients and validation with gold standard invasive measurements. The relevance of the project to the FY10 PRMRP topic of epilepsy stems from the potential use of a validated, network paradigm as a biomarker of risk for the transition from TBI to epilepsy with the intent of interrupting that transition.

## BODY

Research accomplishments are summarized below along the lines of The Statement of Work, which outlined the following main tasks:

- Develop a partial differential equation (PDE)-based tractography methodology to enable fast, whole-brain measurements of connectivity.
- Validate noninvasive measurements of connectivity by comparison to gold standard, invasive electrophysiology measurements.
- Summarize and publish results.

### **Develop a partial differential equation (PDE)-based tractography methodology to enable fast, whole-brain measurements of connectivity.**

The theoretical framework and tests of PDE-based tractography have been published in a high impact journal (1). The results go beyond a previously-published conference paper (2) as follows:

- Clarification of the formalism through diagrams.
- Demonstration of efficacy of PDE formalism when using multi-voxel target regions, as opposed to single-voxel regions, setting the stage for fast whole-brain tractography.
- Demonstration of PDE formalism in a wide range of pathways, including corticospinal, arcuate and short association fibers.
- Demonstration of speed advantage as compared with Monte Carlo and graph theory based approaches.

Additional work clearly demonstrates the comparability of Monte Carlo and PDE approaches in the pathway connecting the posterior cingulate and entorhinal cortex despite a 12,000 times acceleration afforded by the PDE approach. Furthermore, a MATLAB package has been developed to implement the tractography.

### **Validate noninvasive measurements of connectivity by comparison to gold standard, invasive electrophysiology measurements.**

PDE tractography measures of connectivity were compared with electrophysiology measurements of cortico-cortico evoked potentials (CCEPS) achieved with stereotactic electrodes (3). The use of stereotactic electrodes avoids some of the coregistration error associated with the use of subdural grids. Results (figure 2) show correlation between PDE tractography measures of connectivity but not with resting-state functional connectivity (4, 5).

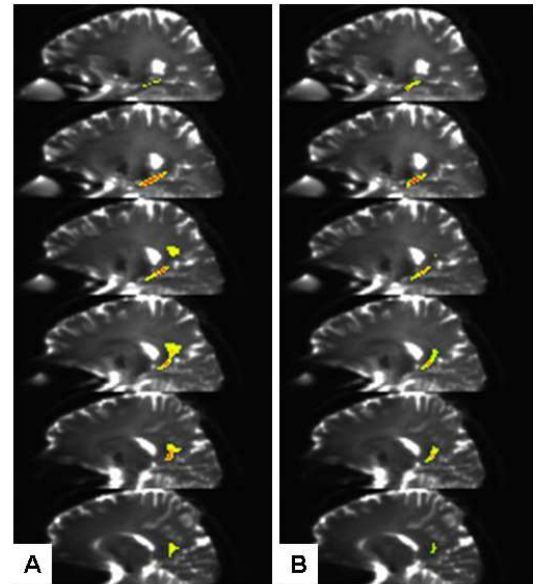


Figure 1. Tractography of pathway connecting posterior cingulate and entorhinal cortex using A) Monte Carlo and B) PDE tractography.

## Summarize and publish results.

Work described here has been published in IEEE Transactions on Medical Imaging (1) and presented at the 2013 Scientific Meeting of the International Society for Magnetic Resonance (3). These are included in the appendix.

## KEY RESEARCH ACCOMPLISHMENTS

- Clarification of the theory of PDE-based tractography.
- Development of a MATLAB package for practical implementation of the PDE approach.
- Finding of correlation between gold-standard electrode recordings and anatomical connectivity based on tractography while no such correlation was found by resting-state functional connectivity.

## REPORTABLE OUTCOMES

- Publication in IEEE Transactions on Medical Imaging (1). Included in the appendix.
- Presentation at the 2013 Scientific Meeting of the International Society for Magnetic Resonance in Medicine (3). Included in the appendix.

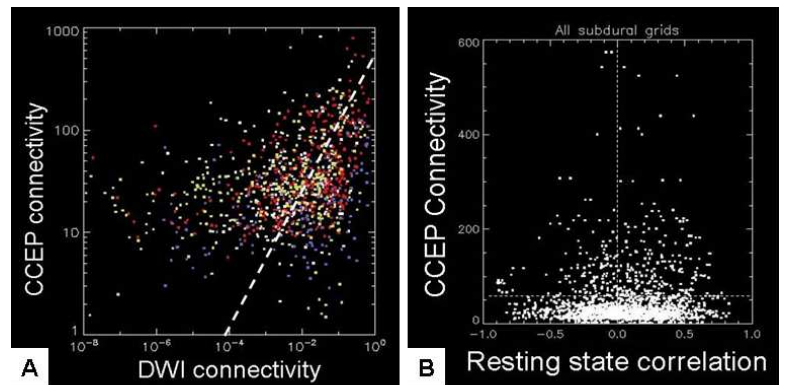


Figure 2. PDE-based connectivity (A) correlates with cortico-cortico evoked potentials (CCEPs) while resting state functional connectivity (B) does not.

## CONCLUSION

The primary goal of this no-cost extension, publishing the results, has been largely achieved with publication of the method in IEEE Transactions of Medical Imaging (1).

We have developed a MATLAB package that can implement the PDE methodology. This package will be tested against Monte Carlo tractography and electrophysiology in a number of pathways. Results to date suggest that PDE-based tractography measures of anatomical connectivity correlate with electrophysiological measures while functional connectivity does not. As the speed of the package enables whole-brain tractography, the product of this research will enable network analyses of anatomical connectivity.

As a scientific or medical product, the work accomplished represents a step towards totally non-invasive evaluation of the brain at risk for epilepsy. Such an evaluation would enable rapid evaluation of pharmacologic interventions and development of new therapies. Unfortunately, although victims of traumatic brain injury are at high risk for developing epilepsy, there is no clear-cut way to predict or evaluate strategies for treating epileptic seizures. On the near term, surgical intervention for pharmacoresistant epilepsy often relies on highly invasive electrode monitoring that is an option for only the most highly motivated patients. Progress toward noninvasive detection of targets for surgical resection would relieve the burden of suffering among these patients while opening up new treatment options.

## REFERENCES

1. Zhang M, Sakaie K, Jones S (2013). Logical Foundations and Fast Implementation of Probabilistic Tractography. IEEE Trans Med Imaging [Epub ahead of print].
2. Zhang M, Sakaie KE, Jones SE. Toward Whole-Brain Maps of Neural Connections: Logical Framework and Fast Implementation. Proceedings 12th IEEE Workshop on Mathematical Methods in Biomedical Image Analysis; 2012; Breckenridge.
3. Jones S, Beall E, Gonzalez-Martinez J, Mathew B, Nair D, Najm I, Phillips M, Sakaie K, Zhang M. Correlation of imaging connectivity with electrophysiological connectivity using intracranial electrodes. Proceedings 21st Scientific Meeting of the International Society for Magnetic Resonance in Medicine. 2013:2142.
4. Biswal B, Yetkin FZ, Haughton VM, Hyde JS (1995). Functional connectivity in the motor cortex of resting human brain using echo-planar MRI. Magn Reson Med, 34(4), 537-41.
5. Lowe MJ, Mock BJ, Sorenson JA (1998). Functional connectivity in single and multislice echoplanar imaging using resting-state fluctuations. Neuroimage, 7(2), 119-32.

# Logical Foundations and Fast Implementation of Probabilistic Tractography

Myron Zhang, Ken E. Sakaie, and Stephen E. Jones

**Abstract**—Although tractography can noninvasively map axonal pathways, current approaches are typically incomplete or computationally intensive. Fast, complete maps may serve as a useful clinical tool for assessing neurological disorders stemming from pathological anatomical connections such as epilepsy. We re-frame tractography in terms of logic and conditional probabilities. The formalism inherently includes global constraints and can compute connections between any two arbitrary regions of the brain. The formalism also lends itself to a fast implementation using standard partial differential equation solvers, which makes whole-brain probabilistic maps of anatomical connectivity feasible. We demonstrate results of our implementation on *in vivo* data and show that it outperforms Monte Carlo approaches in both computation time and identification of pathways.

**Index Terms**—Diffusion MRI, probabilistic tractography, connectome, diffusion tensor imaging, connectivity analysis

## I. INTRODUCTION

TRACTOGRAPHY is the only method that can noninvasively map axonal pathways in the brain [1]–[4]. Current methods are typically incomplete or computationally intensive. For example, standard deterministic streamline tractography typically fails to delineate known lateral projections of the corticospinal tract (CST) [5], [6] or transcallosal connections between hand areas of the motor cortex [7]. Probabilistic tractography [8], [9] can overcome such limitations by generating multiple paths over a probability distribution but can be computationally intensive. Furthermore, most algorithms use only *local* information. That is, each step along a pathway is only determined by information at the position of that step, ignoring knowledge about distal regions.

We introduce a generic formalism for tractography based on probability theory. The formalism inherently includes *global* information about the terminations of pathways and the presence of boundaries. The formalism also lends itself to fast implementation by standard numerical solvers for partial differential equations (PDE). After a theoretical derivation of the formalism, we demonstrate advantages in terms of speed

and identifying pathways that are otherwise difficult to delineate. The advantages are particularly evident when assessing long pathways, such as transcallosal connections between hand motor regions, pathways not lying along major tracts, such as the arcuate fasciculus and pathways near boundaries, such as U-fibers connecting cortical regions along gyri.

The proposed method uses probability theory differently from previous constructions. Standard formulations of probabilistic tractography generate an ensemble of tracks [8], [9]. A connectivity map is generated by showing the number of tracks in each voxel. A given track in the ensemble consists of a sequence of line segments that connect to form a streamline. The line segments initiate at a seed point, the direction of each segment is generated in a probabilistic fashion, and the streamline terminates upon encountering a stopping criterion. Furthermore, the probability distributions at each voxel are derived and sampled using only local information. For example, the direction of a given segment is not influenced by whether or not subsequent segments intersect a target region of interest.

The method proposed here focuses on the expected number of tracks passing through each voxel, rather than the trajectory of segments along the track, from a probabilistic standpoint. Tracks are not explicitly generated, but the number of tracks is required to be continuous. Furthermore, the local information from imaging data is conditioned by requiring all the implicit tracks to intersect both a seed and target region and avoid the tissue boundary. As standard probabilistic tractography generates populations of tracks by random sampling methods, we will refer to it as Monte Carlo (MC) tractography. The method introduced here, implemented with PDE techniques, will be referred to as PDE tractography.

Although the PDE approach was designed to mimic the behavior of track counts generated from MC tractography, the resulting formalism bears some similarity to graph-based shortest path [10], [11] and flow-based approaches [12], [13]. Differences with regard to interpretation and performance among the approaches will be examined with direct comparison of results demonstrated with the graph-theoretic approach [10].

## II. THEORY

The goal is to calculate the number of tracks in a given voxel subject to the conditions that the tracks leave a seed region and terminate in a target region before intersecting a

Copyright (c) 2010 IEEE. Personal use of this material is permitted. However, permission to use this material for any other purposes must be obtained from the IEEE by sending a request to pubs-permissions@ieee.org.

This work was supported by Department of Defense grant PR100438, Citizens United for Research in Epilepsy (CURE) grant 1201SJ, and Neuroimaging Educational Research Fund grant NERF1004SJ.

M. Zhang, K. E. Sakaie, and S. E. Jones are with the Imaging Institute, Cleveland Clinic Foundation, Cleveland, OH 44195 USA (e-mail: mz242@cornell.edu; sakaiek@ccf.org; jones19@ccf.org).



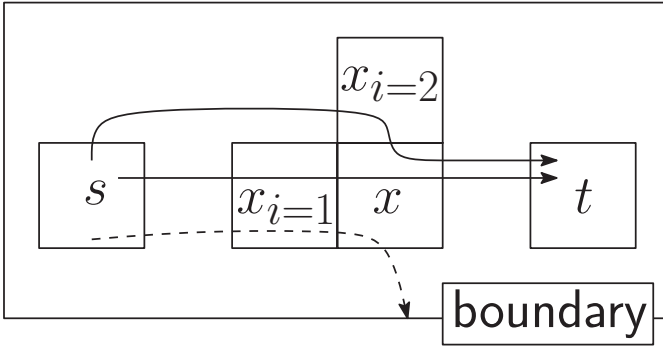


Fig. 1. Illustration of notation. Tracks passing through a voxel,  $x$ , pass through a neighbor voxel,  $x_i$ . For clarity, only two neighbors are shown. Solid lines indicate tracks originating in a seed voxel,  $s$ , and terminating at a target voxel,  $t$ , without intersecting the boundary. Dashed line indicates a track that hits the boundary before reaching the target. Although all tracks satisfy the condition  $X_iX$  (track passes through neighbor  $x_i$  before entering  $x$ ), only the tracks indicated by solid lines satisfy the condition  $X_iT$  (track terminates at target).

boundary. To achieve this goal, we will first develop a generic formalism for considering the track number from the standpoint of conditional probabilities and logic. We will then relate this formalism to diffusion MRI data and a practical algorithm for calculating the number of tracks.

The notation follows conventions for conditional probabilities that have been used in other treatments of the tractography problem [8], [14].  $p(A|B, C)$  denotes the probability of proposition  $A$  given the condition that propositions  $B$  and  $C$  are true. The comma represents the logical AND operation. The derivation uses the product rule [15]:

$$p(A, B|C) = p(A|B, C)p(B|C). \quad (1)$$

We will use lowercase letters to indicate voxels and uppercase letters to indicate conditions. For example,  $t$  indicates a target voxel,  $x$  a voxel along a track and  $x_i$  a neighbor of  $x$ .  $X_iT$  indicates the proposition that a track at voxel  $x_i$  eventually reaches the target voxel,  $t$ , and  $X_iX$  indicates the proposition that a track moves from voxel  $x_i$  to  $x$  (Fig. 1). In addition, we define  $\phi(x)$  as the number of tracks at voxel  $x$ .

Continuity arguments lead to the central equations for the derivation. The number of tracks in a voxel is directly related to the number of tracks in neighboring voxels:

$$\phi(x) = \sum_i p(X_iX|X_iT, I)\phi(x_i), \quad (2)$$

which states that tracks in a voxel,  $x$ , arrive via a neighboring voxel,  $x_i$  and that only tracks terminating at the target,  $t$ , are considered. The relation is through the transition probabilities,  $p(X_iX|X_iT, I)$ , of a track moving from a neighbor,  $x_i$ , to the voxel  $x$  subject to the condition,  $X_iT$ , that the track eventually reaches the target. The symbol  $I$  denotes all prior information, including the implicit condition that the tracks start at a seed voxel and do not intersect a boundary. The conditions introduce *global* constraints by enforcing tracks to intersect the target. In a typical derivation, only *local* transition probabilities, dependent only on properties at the voxel  $x$  and the position of its neighbor,  $x_i$ , would be used without any inherent conditions regarding the target or boundary.

To calculate the global transition probabilities in (2), we first solve for  $p(XT|I)$ . These probabilities are also subject to

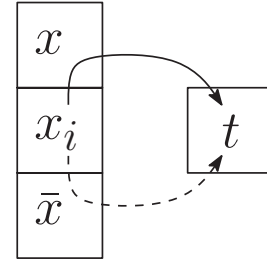


Fig. 2. Illustration of joint probabilities in (5). Tracks passing through voxel  $x_i$  will pass through a neighbor voxel,  $x$ , or some other voxel, represented by  $\bar{x}$ . Tracks represented by both lines satisfy the condition  $X_iT$ . However, only tracks represented by the solid line satisfy the joint condition  $X_iX, X_iT$ , which is therefore equivalent to the joint condition  $X_iX, XT$ .

a continuity condition:

$$p(XT|I) = \sum_i p(XX_i|I)p(X_iT|I), \quad (3)$$

and involve the *local* transition probability of moving from  $x$  to  $x_i$ ,  $p(XX_i|I)$ . These local transition probabilities are derived from the diffusion MRI data. The approach specified here involves integration over a fiber orientation distribution function (fODF) [16]. The fODF is integrated, on a voxel-by-voxel basis, over sub-regions of the unit sphere nearest a line connecting the center of a voxel with each neighbor voxel. Details are provided in the Methods section. If a diffusion orientation distribution function (dODF) [17]-[19] is used instead, the resulting map describes the anisotropic random walk of water molecules.

Equations (2) and (3) are finite difference equations for which a number of standard and fast numerical solvers exist. Solution requires us to specify the transition probabilities  $p(X_iX|X_iT, I)$  to solve for  $\phi(x)$  in (2) and  $p(XX_i|I)$  to solve for  $p(XT|I)$  in (3).

We will now use logical considerations to derive the global transition probability,  $p(X_iX|X_iT, I)$ . From the product rule (1), we find:

$$p(X_iX|X_iT, I) = \frac{p(X_iX, X_iT|I)}{p(X_iT|I)}. \quad (4)$$

Physical considerations (Fig. 2) lead to the relation:

$$p(X_iX, X_iT|I) = p(X_iX, XT|I). \quad (5)$$

Although proposition  $X_iX$  is not independent from proposition  $X_iT$ , propositions  $X_iX$  and  $XT$  are independent if we assume the transition process is Markov, so:

$$p(X_iX, XT|I) = p(X_iX|I)p(XT|I) \quad (6)$$

Inserting (6) into (4), we find:

$$p(X_iX|X_iT, I) = \frac{p(X_iX|I)p(XT|I)}{p(X_iT|I)}. \quad (7)$$

Given the local transition probabilities,  $p(X_iX|I)$ , one can solve (3) to derive  $p(XT|I)$ . One can then derive the global transition probabilities with (7) and then solve for the track number,  $\phi(x)$ , in (2).

Essential to solving the finite difference equations (2) and (3) is the proper selection of boundary conditions. For (2):

$$\phi(b) = 0 \quad (8)$$

$$\phi(s) = N \quad (9)$$

where the number of pathways at the boundary,  $b$ , is set to zero and number of pathways at the seed voxel,  $s$ , is set to a number  $N$ . These conditions directly reflect physical constraints.  $N$  represents the number of tracks originating at the seed that subsequently reach the target without hitting the boundary.  $N$  acts as an overall scaling factor for the number of tracks,  $\phi(x)$ , found at each voxel in the imaging volume. For example, if we set  $N = 100$  and  $\phi(x) = 20$ , that means 20% of the tracks between  $s$  and  $t$  pass through  $x$ . In all of our results, we set  $N = 1$ , so that  $\phi(x)$  represents the fraction of tracks passing through  $x$ . We refer to this scaled track number as “track density.”

For (3), we have:

$$p(BT | I) = 0 \quad (10)$$

$$p(TT | I) = 1. \quad (11)$$

The first condition excludes tracks at the boundary. The second is required by consistency—tracks at the target clearly reach the target. We also impose the constraints:

$$p(TT_i | I) = 0 \quad (12)$$

$$p(S_i S | I) = 0 \quad (13)$$

for all neighbors  $t_i$  of the target,  $t$ , and neighbors  $s_i$  of the seed,  $s$ , when solving (2). Equation (12) reflects the fact that tracks do not emanate from the target, while (13) prevents tracks from returning to the seed after they have left the seed.

The final mathematical expressions for numerical computation of (2) and (3) are two large, linear systems of finite-difference equations, which can be written as square matrices whose size is determined by the number of computational voxels used to represent the brain volume. Since the value of any given voxel is determined solely by the values of adjacent voxels, the matrices are sparse. The equations are finite-difference forms of PDEs [20], suggesting that, in the continuum limit, they could be derived from a PDE.

### III. METHODS

We compare the PDE approach to a Monte Carlo approach and a shortest path approach with *in vivo* data. Tracking performance is evaluated by comparing the similarity of track density maps and track geometries between the approaches and by comparing computation time. We also construct a digital phantom to evaluate discretization error and demonstrate key conceptual and performance points in the PDE method.

#### A. In Vivo Data

*In vivo* data were acquired under a protocol approved by the local internal review board. Five subjects were imaged on a Siemens TIM Trio (Siemens Medical Solutions, Erlangen, Germany) with a standard 12-channel head coil. The HARDI acquisition provided whole-brain coverage with 2.5 mm isotropic voxels (256 mm x 256 mm FOV, 102 x 102 matrix, 48 slices. TE = 77 msec, TR = 6500 msec, BW = 1442 Hz/pixel, partial Fourier factor = 5/8, 61 non-collinear diffusion-weighting gradients with robust ordering [21] with  $b = 1000 \text{ sec/mm}^2$  and 7  $b = 0$  volumes, 2 averages). Motion correction was performed with an iterative algorithm [22] that

updated gradient vectors [23].

For *in vivo* data, seed and target points were placed to examine several important pathways. Shown here are results from corticospinal tract, transcallosal pathway between hand regions of motor cortex, arcuate fasciculus, superior longitudinal fasciculus, and a short association fiber (U-fiber). The length of and presence of multiple fiber crossings along the transcallosal pathway between hand regions of motor cortex make this pathway hard to define, even by probabilistic tractography. The arcuate fasciculus constitutes the inferior margin of the superior longitudinal fasciculus. Each of these pathways can be challenging to identify by tractography due to their length and proximity to the boundary. The superior longitudinal fasciculus and short association fiber are used to compare utility of the PDE method in long and short association pathways.

In all tracts other than the corticospinal tract, a single-voxel seed and target was used to define the pathway. For the corticospinal tract, both single-voxel and multi-voxel regions were used to demonstrate the extensibility of the PDE method to multi-voxel seeds and targets. The seed included 569 voxels in the motor strip, segmented by FreeSurfer [24], and the target included 4 voxels in the brainstem.

All *in vivo* tractography (PDE, MC, and shortest path) was performed with a white matter mask, generated with SPM [25], to define boundaries. For the PDE tractography to run, all that is needed, in principle, is a tissue mask to define boundaries and transition probabilities defined within the mask. In practice, however, implausible connections through, for example, ventricles or across the midsagittal fissure may occur.

#### B. Digital Phantom

Sampling of the fiber orientation distribution along 26 directions, as opposed to a continuum of directions, will lead to discretization error when the fiber orientation lies oblique to the imaging grid. To examine the effect of discretization error, we constructed a simple digital phantom simulating a single straight white matter fiber in the midst of gray matter. The fiber is aligned in the axial plane at angles with respect to the right-left axis ranging from  $0^\circ$  to  $45^\circ$ . The signal profile of white matter, as a function of diffusion weighting gradient, is that of an axially symmetric diffusion tensor with fractional anisotropy (FA) of 0.707 and mean diffusivity (MD) of  $0.7 \times 10^{-3} \text{ mm}^2/\text{sec}$  with principal eigenvector aligned along the fiber. The signal profile of gray matter is that of isotropic tissue (FA = 0, MD =  $0.7 \times 10^{-3} \text{ mm}^2/\text{sec}$ ). Due to symmetry, properties for angles ranging from  $90^\circ$  to  $45^\circ$  will be the same as angles from  $0^\circ$  to  $45^\circ$ .

The length of the fiber was fixed at 52 voxel-widths, and the width and thickness at 1 voxel-width. The simulated data has matrix size and diffusion gradient profile similar to that of the *in vivo* data, with dimensions of  $103 \times 103 \times 48$  voxels. The white matter fiber was centered in the 24th axial slice. The computational mask was one voxel inward from all faces of the data matrix ( $101 \times 101 \times 46$  voxels), which included the white matter fiber and all surrounding gray matter. As



multiple  $b = 0$  volumes are used to counteract the impact of noise for *in vivo* data and no noise was injected in the simulation, the gradient profile used in the simulations used only a single  $b = 0$  image volume.

In addition to evaluating discretization error, the  $0^\circ$  phantom was also used to illustrate  $p(XT|I)$  from (3) and the importance of conditioning the probabilities by solving (2) with conditioned and unconditioned transition probabilities. Also, the  $0^\circ$  phantom was constructed at different resolutions, ranging from  $26 \times 26 \times 12$  to  $208 \times 208 \times 96$ , to evaluate how the speed performance of the PDE method scales with resolution.

### C. Tractography

For the PDE method, local transition probabilities were calculated from the fiber orientation distribution calculated in each voxel of *in vivo* data. The fiber orientation distribution function (fODF) was calculated from the HARDI data by spherical deconvolution [16] with automatically optimized regularization [26]. The resulting fODF is represented as coefficients of a subset of spherical harmonics that satisfies conditions of antipodal symmetry and real, as opposed to complex, values [27]. Spherical harmonics up to degree 8 were used, leading to 45 coefficients. The calculation results in a model for the orientation of white matter fibers in each voxel:

$$\text{fODF}(\theta, \phi) = \sum_{l,m} c_{lm} Y_l^m(\theta, \phi) \quad (14)$$

where  $\theta$  is the zenith angle,  $\phi$  is the azimuth angle,  $Y_l^m(\theta, \phi)$  are the modified spherical harmonics and  $c_{lm}$  are the coefficients specific to a given voxel. The transition probabilities are the integral of the fODF over a sub-region of the unit sphere:

$$p(X_i X | I) = \iint \text{fODF}(\theta, \phi) d\theta d\phi \quad (15)$$

where the integration ranges over the sub-region closest to the vector connecting the centers of voxels  $x$  and  $x_i$ . We perform this integral numerically by calculating values of the fiber orientation distribution over 2000 evenly spaced points on the unit sphere generated by an Archimedian spiral (<http://www.math.niu.edu/~rusin/known-math/97/spherefaq>) and summing values among points nearest the unit vector pointing to each of 26 near neighbor voxels.

The finite difference equations (2) and (3) were solved by numerical solution of a large sparse matrix equation using the *bicgstab* function in MATLAB (The Mathworks, Natick MA). Successive over-relaxation was also used, resulting in equivalent results but requiring substantially more time.

To demonstrate the importance of including global information via conditional probabilities, track counts were calculated in a phantom using local transition probabilities only. Specifically, in (2), the conditional probabilities,  $p(X_i X | X_i T, I)$ , are replaced by the local transition probabilities,  $p(X_i X | I)$ .

To compare the PDE method to a MC method, we used an existing MC algorithm based on fiber orientation distributions [7] adapted from [28]. One billion tracks were initiated from the seed point with direction chosen from the fiber orientation distribution by rejection sampling. The step length was chosen

as 0.75 times the voxel length (1.875 mm), as in the work of Hagmann *et al.* [28] and in Lowe *et al.* [7]. No optimization with regard to step length was performed in this work. Steps with a bending angle of more than  $90^\circ$  were reflected across the origin to limit backtracking. Streamlines were eliminated if they encountered the boundary or returned to the seed before reaching the target. Computation was performed using in-house software written in C and implemented on a 320-cpu cluster.

We also demonstrate results generated from code generously provided by Dr. Iturria-Medina for comparison with graph-based shortest path approaches [10]. The code takes an input of connectivity between each voxel and its 26 neighbors, for which we use the same discretized fODF values as we do for the PDE method. The same mask was used as for all approaches.

For the PDE and MC methods, the entire calculation entails 1) calculation, discretization and loading into memory of the fODF, 2) calculation of the track density maps and 3) saving the maps to disk. Additionally, in the MC calculation track density maps generated by each CPU of the cluster are merged in a separate step. Quoted PDE and MC calculation times are only for step 2, calculation of track density maps. Step 1 requires several minutes, but need only be done once for a given data set. Step 3 requires several seconds. Merging results for the MC calculation from the cluster requires several minutes.

For the shortest path method, the entire calculation entails 1) calculation, discretization and loading into memory of the fODF, 2) generating the graph representation of the brain, 3) computation of shortest paths using Dijkstra's algorithm and 4) saving the maps to disk. The reported shortest path computation times are only for step 3, computation of shortest paths using Dijkstra's algorithm.

## IV. RESULTS

First, we examine discretization error, intermediate steps of the theory and the effect of conditioning transition probabilities in a single-fiber digital phantom. We then present results of PDE, MC and shortest path tractography in a variety of *in vivo* pathways. Lastly, we evaluate the speed performance of PDE and shortest path tractography in increasingly large datasets.

### A. Phantom Evaluations

Figs. 3 and 4 show the impact of discretization error on track density values. Track densities were calculated for the digital phantom for each integer angle between  $0^\circ$  and  $45^\circ$  with respect to the right-left axis. Fig. 3 shows track density maps for angles of  $0^\circ$ ,  $22^\circ$  and  $45^\circ$ , from which we can see that the results are qualitatively similar. To make a quantitative comparison, a line was drawn between the center of the seed and target voxels for each angle, and values of track density in each voxel intersecting the line were then assigned a position coordinate ranging from 0 (center of seed) to 1 (center of target). To facilitate comparison with the  $0^\circ$  configuration, linear interpolation was used to determine

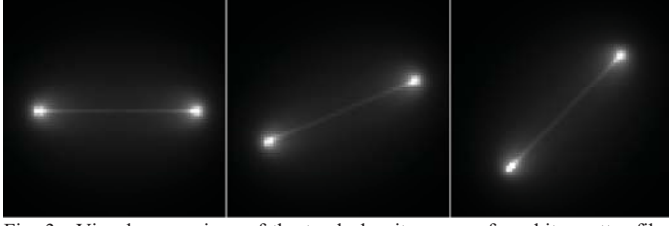


Fig. 3. Visual comparison of the track density maps of a white matter fiber phantom rotated at 0°, 22°, and 45° with respect to the right-left axis in the axial plane. The intensity range is set to [0, 0.2].

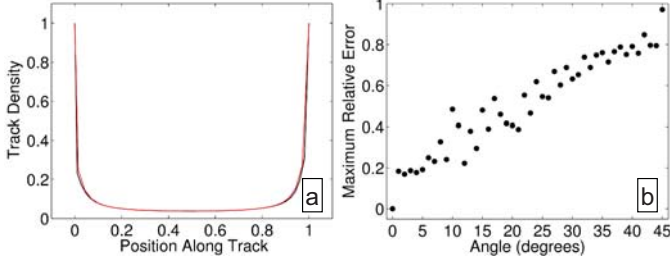


Fig. 4. (a) Track density along simulated white matter fibers oriented along the right-left axis (black) and in the axial plane at a 45° with respect to the right-left axis (red). Fiber is 1 voxel in cross section. Position along the track is scaled so that the seed is positioned at zero and the target is positioned at 1. (b) Maximum relative error of track density as a function of angle. The size of error can be large, but this may be largely attributed to finite sampling and linear interpolation along a very steep, nonlinear curve, as seen in (a).

values at 1000 equally-spaced points from 0 to 1. Fig. 4(a) shows the profile of track densities for 0° and 45°. Qualitatively, the difference is slight. We quantify the difference in track density  $\phi$ , as defined in (2), by calculating the maximum relative error at angle  $\theta$

$$\max_t \left( \left| \phi(t, \theta) - \phi(t, 0) \right| / \phi(t, 0) \right), \quad (16)$$

where  $t$  is the position coordinate and  $\theta$  is the angle with respect to the right-left axis. The maximum relative error is largest for  $\theta = 45^\circ$  (Fig. 4(b)). The size of the error can be large and occurs where the track density exhibits a steep slope near the seed and target. The error may therefore result from finite sampling and linear interpolation of track density values along the length of the pathway. The cross section of the fiber in the simulation shown is 1 voxel. However, fibers with larger cross sections show similar trends of comparable magnitude, indicating that the discretization error is inherent to the algorithm, not the fiber geometry.

The 0° phantom was also used to demonstrate the results of solving intermediate step (3) for  $p(XT | I)$  (Fig. 5). The value at each voxel  $x$  represents the probability that a track from  $x$  will intersect the target but not the boundary. The intensity is high near the target but falls off quickly with distance from the target. The rapid falloff reflects the low likelihood of tracks reaching the target before the boundary, a result of the boundary (the 6 faces of the imaging volume) being much larger than the target (a single voxel). The map resembles a solution of Laplace's equation with boundary conditions of 1 at the target and 0 on the faces of the volume. However, anisotropy in the white matter fiber leads to an oblong shape in contours, particularly near the target. The value at the seed,  $p(ST | I)$ , is only  $3.19 \times 10^{-4}$ . Only about 3 out of every 10,000 tracks will reach the target from the seed without intersecting

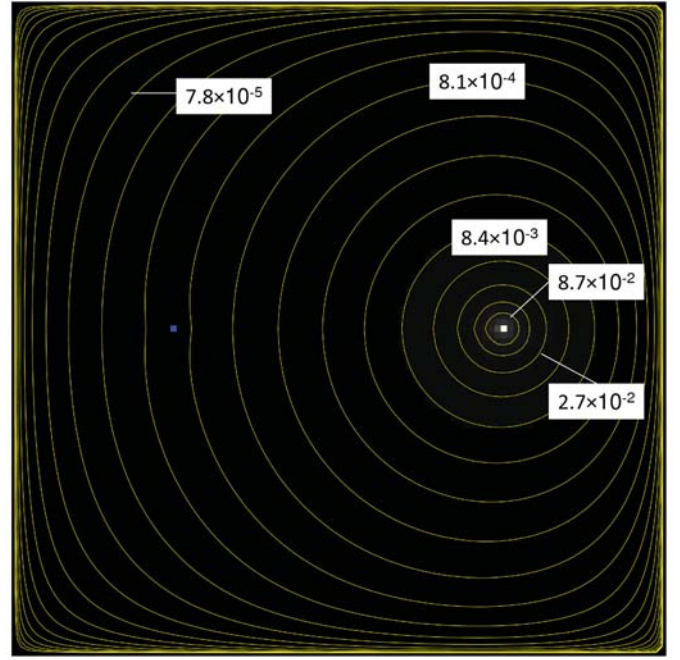


Fig. 5. The solution to (3),  $p(XT | I)$ , in the 0° white matter fiber phantom. The intensity range is [0, 1]. The brightest white dot is the target, the blue dot represents the seed and the boundary sits at the faces of the imaging volume, including the edges of the figure. Values fall rapidly with distance from the target. Oblong shapes of contours near the target indicate effects of white matter anisotropy.

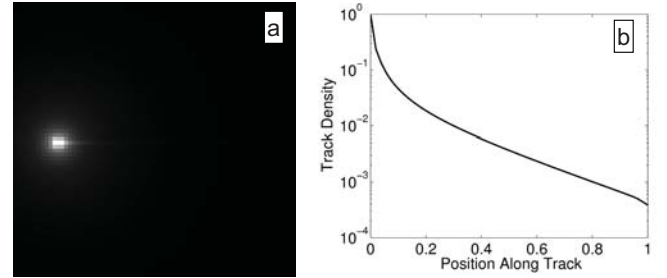


Fig. 6. (a) Track density map for white matter fiber phantom using unconditioned probabilities in the continuity equation (2). The intensity range is [0, 0.2]. The track density appears isotropic due to the rapid falloff in density in the absence of conditioning. The anisotropy of the fiber can be barely discerned to the right of the seed. (b) Semi-log plot of track density versus position along the white matter fiber without conditioning on the target. Position 0 is at the seed while 1 is at the target.

the boundary. Conditioning on the target in (2) limits consideration to only the small subset of tracks that reach the target before hitting the boundary.

Fig. 6 shows the results of solving the continuity equation (2) using the *unconditioned* transition probabilities using the same 0° phantom. Conceptually, this is equivalent to starting tracks from the seed and then considering all tracks regardless of whether they intersect the target or boundary. In the track density map (Fig. 6(a)), we can see anisotropy along the white matter fiber in voxels close to the seed, but as the tracks fan out, the track density decreases rapidly with increasing distance from the seed and fails to rise back up at the target. A semi-log plot of track density along the line from seed to target is shown in Fig. 6(b). The conditional probabilities effectively filter out the tracks that strike the boundary or do not reach the target, leading to a more focused track density

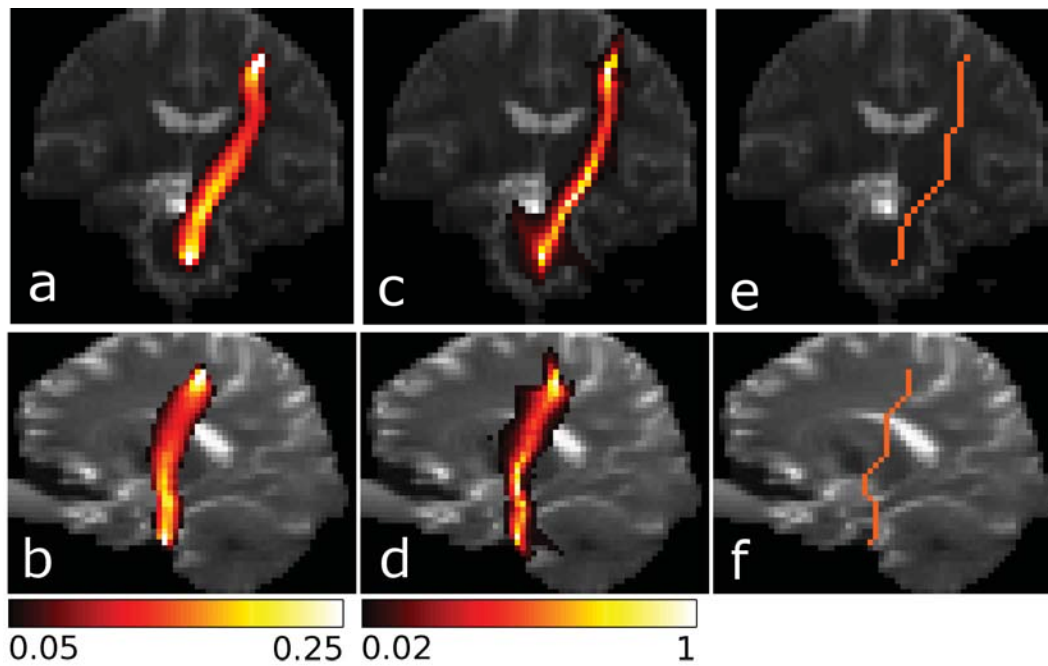


Fig. 7. Maximum intensity projection of the corticospinal tract generated by PDE (a, b), Monte Carlo (c, d), and shortest path (e, f) methods. Intensity ranges were set to  $\varphi \in [0.05, 0.25]$  (a, b) and  $\varphi \in [0.02, 1]$  (c, d), with corresponding color map shown at the bottom. Subsequent figures will only report intensity ranges for  $\varphi$ , with the same color map implied.

TABLE I  
RELATIVE PERFORMANCE OF PDE, SHORTEST PATH (SP), AND MONTE CARLO (MC) TRACTOGRAPHY.

Pathway	CPU-seconds (PDE)	CPU-seconds (SP)	CPU-seconds (MC)	Track Efficiency (MC)
Arcuate	1.4	8.4	$4.3 \times 10^6$	$1.4 \times 10^{-8}$
Transcallosal	1.1	8.7	$3.6 \times 10^6$	$1.1 \times 10^{-7}$
Longitudinal Fasciculus	0.89	7.7	$4.3 \times 10^6$	$1.0 \times 10^{-8}$
Short U-fiber	0.88	7.4	$4.4 \times 10^6$	$6.8 \times 10^{-4}$
Corticospinal (single-voxel)	1.2	9.1	$4.6 \times 10^6$	$2.7 \times 10^{-6}$
Corticospinal (multi-voxel)	1.1	N/A	$1.6 \times 10^6$	$2.1 \times 10^{-5}$

For Monte Carlo results,  $10^9$  tracks were generated at the seed for each pathway, and track efficiency denotes the fraction of those tracks that terminated at the target. Comparison with multi-voxel seed and target was only performed for PDE and MC tractography on the corticospinal tract.

profile that can persist over long distances (Figs. 3 and 4).

### B. Anatomical Results

Table I summarizes the computation times of the PDE, MC, and shortest path methods in the examined pathways. We can clearly see the performance advantage of PDE tractography as compared with MC tractography. One billion tracks were seeded for each pathway in MC tractography. The tracking efficiency, or fraction of tracks leaving the seed voxel that eventually reach the target voxel, is remarkably low for MC tractography, requiring use of a large computing cluster to gain any number of tracks, particularly for pathways near the boundary between gray and white matter (arcuate fasciculus) and for long pathways with numerous fiber crossings (transcallosal motor pathway). The computation time is concomitantly large, on the order of 1 CPU-month. While the metric of

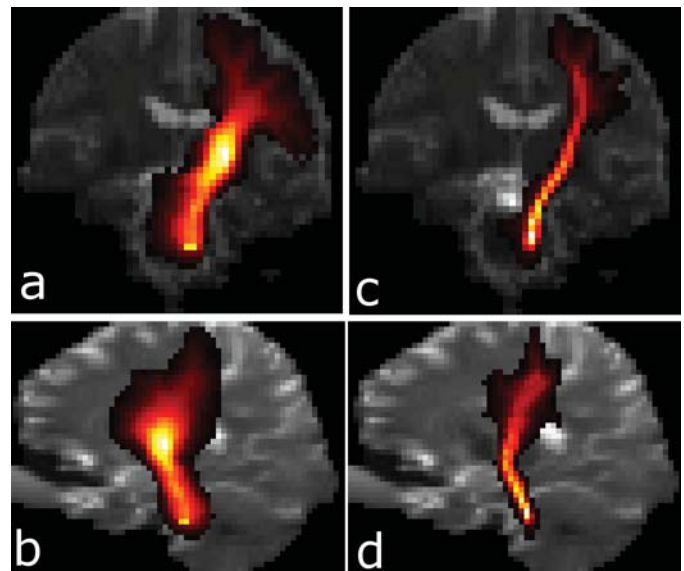


Fig. 8. PDE (a, b) and Monte Carlo (c, d) tracking between multi-voxel seed and target regions. Maximum intensity projections are shown of tracking between a seed ROI in the motor strip (569 voxels) and target ROI in the brainstem (4 voxels). Intensity range is set to  $[0.01, 1]$  for all images.

tracking efficiency is not directly applicable to the PDE approach, run time is uniformly on the order of 1 second for any given pathway, in a computational brain volume of 65,000 voxels. The shortest path approach requires less than 10 seconds in the same brain volume for any pathway.

Fig. 7 compares PDE, MC, and shortest path tractography within a readily defined pathway, the corticospinal tract connecting brainstem and the hand knob of the right motor cortex. Shown are maximum intensity projections of the track density from the PDE and MC methods and the maximum likelihood path from the shortest path method. This pathway typically poses few difficulties for tractography, and we find



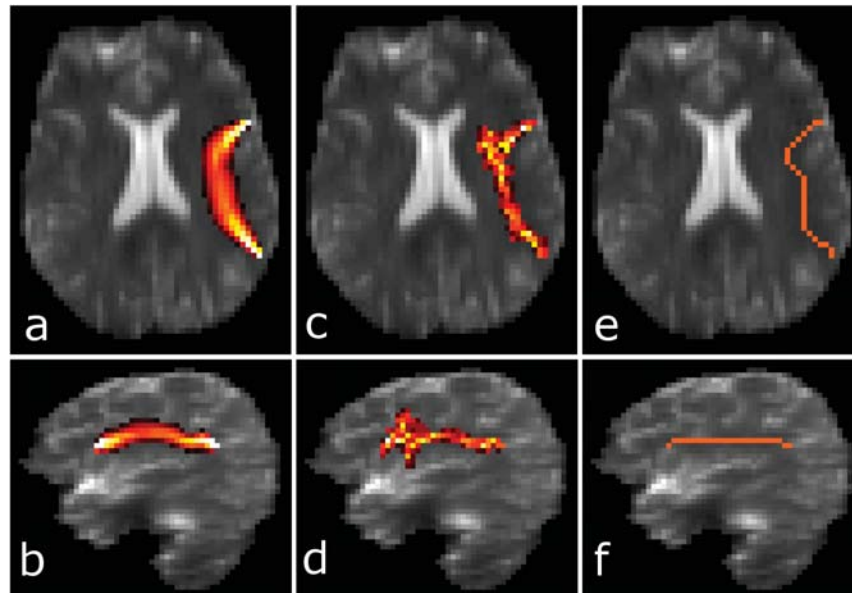


Fig. 9. Maximum intensity projection of the arcuate fasciculus generated by PDE (a, b), Monte Carlo (c, d), and shortest path (e, f) methods. Intensity ranges were set to [0.05, 0.3] (a, b) and [0.01, 1] (c, d).

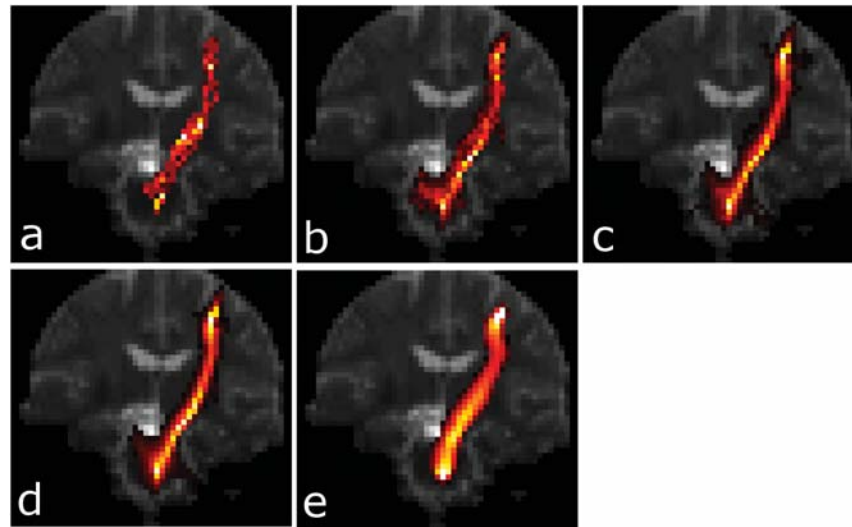


Fig. 10. Comparison of maximum intensity projections of the corticospinal tract with Monte Carlo seeding  $10^6$  (a),  $10^7$  (b),  $10^8$  (d),  $10^9$  (d) tracks, and the PDE result (e). Intensity ranges were set to [0.02, 1] (a-d) and [0.05, 0.25] (e). As more tracks are seeded, the Monte Carlo results appear smoother, approaching the PDE result.

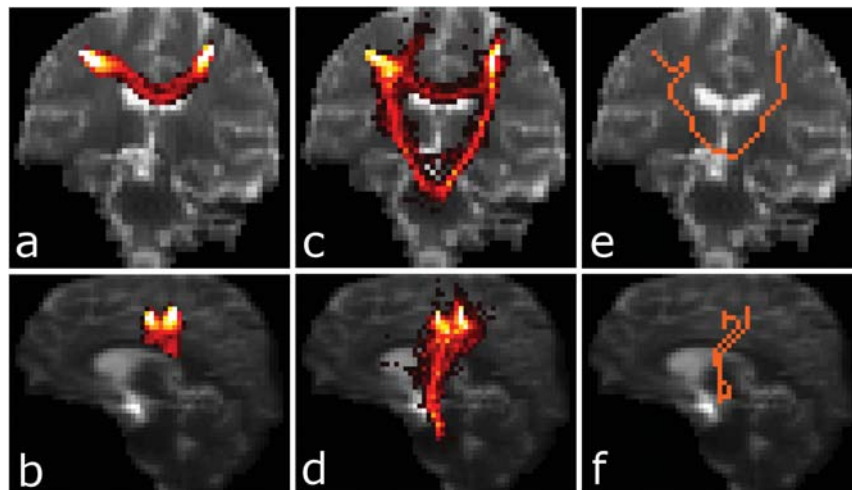


Fig. 11. Maximum intensity projection of the transcallosal pathway generated by PDE (a, b), Monte Carlo (c, d), and shortest path (e, f) methods. Intensity ranges were set to [0.05, 0.7] (a, b) and [0.01, 1] (c, d). Monte Carlo and shortest path methods show a false connection through the pons, which is absent in the PDE result.

that the resulting track shapes from PDE (Fig. 7(a), (b)), MC (Fig. 7(c), (d)) and shortest path (Fig. 7(e), (f)) methods are similar.

The single-voxel seed and target defining the corticospinal tract above can be replaced by multiple-voxel regions without loss of generality or performance in the PDE approach. For example, Fig. 8 shows the corticospinal tract connecting a seed region with 569 voxels in motor cortex and 4 voxels in brainstem. The PDE computation time was the same as that required for the seed and target consisting of single voxels (Table I). The track density map shows details of intersection with motor cortex (Fig. 8(a), (c)) that are not apparent in the single-voxel seed/target case (Fig. 7(a), (c)). The PDE and MC results appear similar, but the PDE result shows more lateral projections of the corticospinal tract which may explain the larger extent of the PDE track density map relative to that of the MC map.

Fig. 9 shows the arcuate fasciculus, which can be difficult to identify because it lies adjacent to gray matter. We can see that the PDE and shortest path results exhibit a similar geometry in the axial view (Fig. 9(a), (e)), but in the sagittal view (Fig. 9(b), (f)), the PDE track curves through axial planes while the shortest path track is flat, mostly restricted to a single axial slice. The MC results (Fig. 9(c), (d)) show a similar geometry to the PDE results (Fig. 9(a), (b)), but in pathways close to the boundary like this one, the majority of tracks generated by the MC method terminate prematurely upon intersecting gray matter, as seen by the patchy appearance of the track counts and the low tracking efficiency (Table I). Only 14 tracks out of a billion seeded terminate at the target.

Qualitatively, the results of the PDE approach are smoother than those from the MC approach. This smoothness may arise from two factors. First, the calculation of local transition probabilities discretizes the fODF, integrating over directions associated with each of 26 neighbors of a given voxel. Such integration smears the fODF with respect to angle, leading to smoothing of resulting track density maps. Second, the PDE approach resembles the limit of the MC approach as the number of samples approaches infinity. It is difficult to disentangle these two causes in general. However, we can demonstrate how the MC results approach the smooth PDE results as the number of MC samples increases. Fig. 10 shows, in the corticospinal tract, how the patchiness of the track density gives way to a smooth profile as the number of samples increases. As the MC approach does not discretize the fODF, the smoothing in this case results exclusively from the approach to infinity. We used the corticospinal tract rather than the arcuate fasciculus for Fig. 10 because the low tracking efficiency of the arcuate requires impractically long computation times to generate a sufficient number of tracks.

Fig. 11 shows advantages of PDE tractography in delineating long pathways encompassing multiple crossings, such as the transcallosal motor pathway. The difficulty of MC tractography in sampling the pathway is again shown by the patchy appearance of the track counts (Fig. 11(c), (d)) as compared to PDE tractography results (Fig. 11(a), (b)).

Furthermore, the MC tractography generates a well-known but artifactual “connection” through the pons, which does not have high track density in the PDE result. This path through the pons is also the maximum-likelihood connection generated by the shortest path approach (Fig. 11(e), (f)).

To evaluate the PDE method in pathways of different length, we performed tractography in long and short association fibers. Fig. A1 (presented in the Appendix) shows the results of tracking the superior longitudinal fasciculus. As in the transcallosal pathway, MC and PDE tractography show differences. As can be seen in Fig. A1, the PDE method traverses the superior longitudinal fasciculus. For the same seed and target, the MC method descends into the inferior longitudinal fasciculus and uncinate fasciculus, connecting with the superior longitudinal fasciculus at the ends. The shortest path method track shows the same geometry as the MC track.

Fig. A2 shows the results of tracking a short U-fiber. Due to the discretization inherent to the method, pathways that are short compared to the voxel dimension may not be as clearly delineated. This can be seen from the difference in appearance between the long (Fig. A1(a), (b)) and short (Fig. A2(a), (b)) tracks. While the features of the superior longitudinal fasciculus are clear, the shape of the U-fiber is harder to discern in the PDE, MC and shortest path methods, which all present results in discrete voxels.

### C. Speed Evaluation

Spatial discretization inherent to the proposed method imposes a strong limitation on spatial resolution. Streamline tractography methods can, in principle, achieve sub-voxel resolution by inferring a continuous vector field of fiber orientations from the discretely sampled field [4]. Such a result may be approximated by the PDE approach by increasing voxel resolution at the acquisition level or by interpolation but with a cost in computation time. To assess the impact of such interpolation, we constructed the 0° phantom at eight different resolutions ( $26r \times 26r \times 12r$ ,  $r = 1, 2, 3, \dots, 8$ ). The  $52 \times 52 \times 24$  voxel phantom had a mask containing  $6.0 \times 10^4$  tissue voxels, approximately equal to that of the *in vivo* tissue mask. The computation time depends on the number of tissue voxels within the mask, not the total number of voxels in the imaging volume. Fig. A3 shows plots of PDE and graph-based computation times against number of tissue voxels in the mask. The run time for the PDE method scales linearly with the number of voxels in the mask, while the run time for the graph-based tracking rises quadratically. Times for the phantom with a mask size approximately equal to that of the *in vivo* mask are also indicated. A fourfold increase in spatial resolution, corresponding to interpolating *in vivo* voxel dimensions from 2.5 mm isotropic to 0.625 mm isotropic, would increase the PDE computation time from approximately 1 second to 4 minutes.

## V. DISCUSSION

We have introduced a theoretical formalism for tractography that inherently accounts for global properties and lends itself to fast implementation. *In vivo* examples demonstrate

advantages in the ability to delineate pathways that are long and that course near boundaries. Furthermore, connections of any two points in the brain can be quantified. While MC tractography may yield zero streamlines between two distal points, one may be left to wonder if the absence of streamlines is due to an absence of connectivity or a failure to generate a large enough ensemble of streamlines. The PDE approach will always give a nonzero, but sometimes small, density of tracks between two points. The MC methods and PDE methods essentially solve the same underlying problem, but with different approaches. Intuitively the increased efficiency of the PDE approach could be appreciated if the MC solution is viewed as a “serial” computation, testing each possible track one after another, whereas the PDE solution is viewed as a “parallel” computation, computing all the possible pathways simultaneously.

The use of probability theory introduced here is inherently different from previously introduced approaches to probabilistic tractography. Our approach is to directly calculate the *number* of pathways in a given voxel using considerations of continuity. Seminal work by Parker [9] and Behrens [8] use probabilistic approaches to govern the trajectories of each of an ensemble of pathways. The probabilistic aspect enters because the step direction along each segment of each streamline is generated by sampling over a probability distribution generated from the diffusion MRI data. Standard streamline tractography can, within this framework, be seen as generating a maximum likelihood streamline from the ensemble. Friman introduced a formalism for calculating the posterior probability of individual streamlines [14]. Similarly, previously-introduced global methods [29], [30] focus on generating individual streamlines. The focus on direct calculation of track counts rather than on generating individual pathways lends itself to fast implementation by numerical PDE methods.

The manner in which the formalism incorporates global information bears some discussion. In typical, local tractography, each step along a streamline is determined using only information at the location of that step, ignoring information from distal points along the streamline. In global tractography, information from distal regions has an influence. Consider, for example, a straight pathway in which the fiber orientation halfway along the path is corrupted by noise, leading to a fiber orientation perpendicular to that of other points along the path. In local tractography, limits on bending angle will terminate tracks when they encounter the noisy voxel. In global tractography, the local fiber orientation information at the noisy voxel is ignored in the construction of a track as long as there is consistency between the fiber orientation and the track direction overall [30]. In other words, the global approach departs from the greedy dominance of local transition probabilities between neighboring voxels. In the formalism presented here, the transition probabilities  $p(X_i X | X_i T, I)$  are constructed from local probabilities,  $p(X_i X | I)$ , that are tempered by the constraints that tracks intersect the target and satisfy the boundary conditions, represented by  $p(XT | I)$  in (7). The values of  $p(XT | I)$  furthermore encode what will

happen at distal voxels. For example, suppose that voxel  $x_i$  has large local transition probability,  $p(X_i X | I)$ , but successive transitions from  $x$  lead tracks away from the target or towards a boundary. Then  $p(XT | I)$  will be small, leading to a small value for  $p(X_i X | X_i T, I)$  despite the large local transition probability.

Although (2) and (3) take the form of finite-difference formulations of PDEs, the equations do not derive from PDEs. It is of some interest, however, to consider which PDEs (2) and (3) might approximate. One interpretation of (3) is the finite-difference form of Laplace’s equation in a warped space. To illustrate, consider, in two dimensions, Laplace’s equation,

$$0 = f_{xx} + f_{yy} \approx \frac{f(x + \Delta x, y) - 2f(x, y) + f(x - \Delta x, y)}{2\Delta x} + \frac{f(x, y + \Delta y) - 2f(x, y) + f(x, y - \Delta y)}{2\Delta y}. \quad (17)$$

Rearranging (17) to isolate  $f(x, y)$  gives

$$f(x, y) \approx [(\Delta y)f(x + \Delta x, y) + (\Delta y)f(x - \Delta x, y) + (\Delta x)f(x, y + \Delta y) + (\Delta x)f(x, y - \Delta y)] / [2(\Delta x + \Delta y)], \quad (18)$$

which can be re-written in a form analogous to (3)

$$f(r) = \sum_i c(r, r_i) f(r_i) \quad (19)$$

where  $r$  corresponds to position  $(x, y)$  and neighbors  $r_i$  corresponds to neighbors  $(x \pm \Delta x, y)$  and  $(x, y \pm \Delta y)$ . The coefficients  $c(r, r_i)$  correspond to a function of the grid spacing, either  $\Delta x / [2(\Delta x + \Delta y)]$  or  $\Delta y / [2(\Delta x + \Delta y)]$ , that varies from voxel to voxel. Other neighbors can be included by considering higher order terms, and the extension to three dimensions is straightforward. When  $\Delta x = \Delta y$ , all coefficients are 1/4, and the finite difference equation directly represents Laplace’s equation. If the coefficients are different for different neighbors and at different voxels, the PDE is equivalent to Laplace’s equation in a warped metric space. This interpretation resembles ideas suggested by others [31]–[33] in different contexts. Note that the coefficients  $c(r, r_i)$  exhibit antipodal symmetry (opposite directions are weighted by the same coefficients). This symmetry is consistent with the coefficients  $p(XX_i | I)$  in (3), which are derived from antipodally symmetric spherical harmonics. The coefficients in (2), however, do not necessarily exhibit antipodal symmetry, so the warped-space interpretation does not apply. We do not know of any commonly used PDE that equivalent to (2).

One implicit parameter of the proposed method is the number of neighbors defined for each voxel. On a three dimensional grid, each voxel has 6 nearest neighbors and 26 adjacent neighbors. The results presented use 26 neighbors. Use of 26 neighbors may raise the concern that the continuity of track number is violated because, when considering transitions among 26 neighbors, a track may traverse more than one neighbor voxel, leading to over-counting. To illustrate, consider the simplified 2-dimensional case (Fig. 12) in which a voxel  $x$  has nearest neighbor  $x_1$  and an adjacent, but not nearest, neighbor  $x_2$ . If we consider just the number of tracks in each voxel, continuity is not satisfied. Voxel  $x$  contains three tracks, but the neighbors contain a total of four



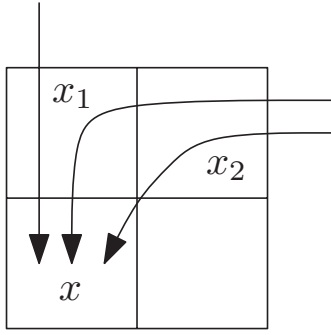


Fig. 12. Illustration of continuity when including non-nearest neighbors. As explained in the text, conditional probabilities avoid over-counting.

tracks, two in  $x_1$  and two in  $x_2$ . However, weighting with the conditional probabilities,  $p(X_i X | X_i T, I)$  in the continuity equation (2) assures that each track is counted only in the neighbor  $x_i$  when the track directly enters  $x$  from  $x_i$ . In the example, all tracks in  $x_1$  enter  $x$  directly, giving  $p(X_1 X | X_1 T, I) = 1$ , while only half of the tracks in  $x_2$  enter  $x$  directly, giving  $p(X_2 X | X_2 T, I) = 1/2$ , resulting in

$$\begin{aligned} \varphi(X) &= p(X_1 X | X_1 T, I)\varphi(X_1) + p(X_2 X | X_2 T, I)\varphi(X_2) \\ &= (1)(2) + (1/2)(2) = 3, \end{aligned}$$

satisfying continuity.

#### A. Adaptability and Extensions

The methods introduced can be readily adapted to incorporate aspects of nearly any existing methodology. For example, the orientation probability distributions generated by FSL's bedpostx program [5], [34] can be used to generate local transition probabilities instead of fODFs generated by spherical deconvolution. Alternatively, counts of streamlines generated by diffusion tensor-based tractography can also be used [10].

The formalism may be extended or modified. Besides using different transition probabilities, the boundary conditions can be altered to specify the derivative of the track count (Neumann boundary conditions) instead of the value (Dirichlet) or a mixture of the two. Specifying the derivative may be more appropriate at boundaries where the tracks are expected to align parallel to the boundary, such as ventricles or brainstem, as opposed to boundaries where the tracks are expected to terminate at the boundary, such as the neocortex.

Our focus on track counts is largely driven by our long-term strategy of defining pathway-dependent statistics for assessing diseased tissue. For example, we have previously assessed anatomical connectivity along the motor pathway by integrating metrics of tissue integrity, such as radial diffusivity, along the pathway [7]. For such a strategy, the parameterized path of individual streamlines is not absolutely necessary, but the number of streamlines in each voxel can be used to generate a weighted mean of tissue integrity along the pathway.

However, it is possible to construct streamlines from the track density maps. The weighted sum of vectors,  $\vec{d}_i$ , pointing from the center of a voxel,  $x$ , to the centers of each of its neighbors,  $x_i$ , yields a vector:

$$\vec{d}(x) = \sum_i p(X X_i | X T, I) \vec{d}_i, \quad (20)$$

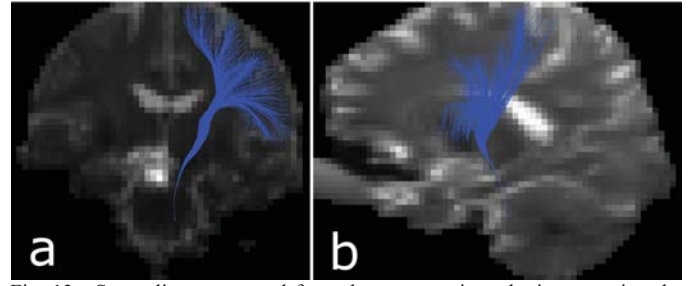


Fig. 13. Streamlines generated from the motor strip to brainstem using the PDE formalism. For display, the 3-dimensional streamlines are projected onto a coronal (a) and sagittal (b) plane.

where the weighting is the conditional probability derived in (7). The vector  $\vec{d}(x)$  can be interpreted as the expectation value of the direction of streamlines. Defining  $\vec{d}(x)$  at each voxel results in a vector field that can be integrated from points in the seed to generate streamlines. The resulting streamlines inherit the conditions inherent to the track density map, such as termination at the target and avoidance of boundaries. An example of streamlines for the corticospinal tract, using the same seed and target regions as Fig. 8, is shown in Fig. 13. Preliminary work suggests that these streamlines avoid unphysical arrangements such as tight bends and multiple visits to the same voxel. Future work will examine such streamlines in more detail.

#### B. Comparison with Other PDE and Graph Methods

A comparison in terms of interpretation can now be made with graph-based shortest path [10], [11] and flow-based approaches [12], [13]. In our PDE formalism, the resulting track count,  $\varphi(x)$ , can be interpreted as the number of tracks in a given voxel,  $x$ , that start at a seed region and terminate at a target region without intersecting a boundary. The interpretation is similar to connectivity values generated by the probtrackx program of FSL [8] if the "--targetmasks" option is used and is the default of the MC algorithm proposed by Lowe *et al.* [7].

The interpretation differs from those of graph-based shortest path methods and flow-based algorithms. Graph-based shortest path methods [10], [11] construct a network of edges between each pair of neighboring voxels. The edge weights are similar, in principle, to the local transition probabilities introduced here. The product of edge weights along a path defines the weight of the path, and the algorithms find the path with maximum weight to define connectivity between a seed voxel and every other voxel. The result differs from the PDE approach because the edge weights are not conditioned on termination at the target and avoidance of boundaries. As only a single path is found between seed and each voxel, the graph-based methods represents a map of maximum likelihood paths, rather than an ensemble of pathways.

Flow-based approaches model fluid-like movement through a vector field derived from the diffusion data. The resulting maps of connectivity are conceived as steady-state flow between a source and sink [12] or the arrival time of a wave front [13]. As the approach of Hageman *et al.* finds a steady state that is consistent throughout the entire vector field, including target and boundary, it bears strong similarity to the

approach introduced here. However, the underlying equations differ. The approach of Hageman *et al.* [12] uses the Navier-Stokes equations, literally modeling water movement through the brain. The approach proposed here considers conservation of track number as the fundamental idea. Front propagation methods do not impose a constraint on reaching a target. Front propagation methods can, however, incorporate some physical constraints in a manner similar to streamline tractography, such as stopping propagation in areas of low fractional anisotropy.

An apparently minor, but quite important difference among methods centers on the explicit definition, or not, of a target. Our proposed algorithm requires definition of seed and target regions to define connectivity. In this sense, connectivity is defined similarly by the approach of Hageman *et al.* [12] and MC approaches in which the target is defined. Such conditioning on the target eliminates distal fading from the seed to the target, as can be seen from the track densities being the same at the seed and target regions (Fig. 4). The other approaches discussed above do not require an explicit target and therefore result in maps of connectivity between a seed region and all other voxels which fades with distance from the seed. For example, in graph-based methods, the probability of a given connection is derived from the product of edge weights along a path. As each edge weight is less than or equal to 1, the probability decreases with path length, and the connectivity maps exhibit distal fading. The graph-based methods will, however, always define a pathway between the seed region and any given voxel even if the connectivity is vanishingly small.

A practical distinction is in terms of speed. Fluid flow approaches may have computation times of hours [12] while our proposed method takes only seconds. The proposed method also compares favorably with graph-based methods, especially on larger computation volumes (Fig. A3). The need to run the computation over numerous seed-target pairs tempers the speed advantage but can be addressed by calculating the result of each pair in a parallel fashion.

### C. Limitations and Uncertainties

The simulation shown in Figs. 3 and 4 demonstrates that discretization error—due to a combination of discretization of the fODF and restriction of results to the discrete imaging grid—induces systematic errors in the estimation of track densities, but none so severe as to cause failure to map a connection. In addition to this systematic error, the restriction of results to a discrete voxel grid can be a liability when mapping pathways that are small compared to the voxel dimension. As seen in Fig. A2, pathways that are small compared to the voxel size are not as conspicuous as longer pathways. Sampling at higher resolution can ameliorate this problem to an extent. However, signal to noise ratio considerations limit acquiring data at spacing finer than approximately 1 mm cubed. Interpolation may also be used but has not been examined with regard to the proposed method. Conversely, the performance of the proposed method is particularly appealing for long pathways. Distal fading of track densities can lead to

excruciatingly long computation times with MC methods for long pathways.

Another limitation related to presenting results in discrete voxels is that the extent of the track density map does not appear as sharp as what one may expect from streamline tractography. As the MC method shows this to a qualitatively similar extent, we believe this appearance stems primarily from the use of voxel-wise track density maps rather than issues such as discretization of the fODF in the calculation of the PDE results.

Unfortunately, our method does not include an automated means of setting thresholds for optimal display of the track density map. The difficulties are illustrated in Fig. A4. Long and short association fibers are shown at different thresholds. Figures with minimum threshold set to zero (Fig. A4(a), (f)) show that PDE tractography always finds a nonzero, but often small, value for track density. Finding a specific threshold that eliminates the implausibly low connectivity values depends largely on the extent of the white matter pathway, as do the differences in how the tract sharpens and diminishes with threshold. The optimal threshold range for the long fiber is lower than that for the short fiber. The value of track density in any given voxel is the fraction of tracks, leaving the seed and hitting the target but not the boundary, that pass through that voxel. As can be seen from Figs. A4(e) and (j), the track density is necessarily high near the seed and target. However, in intervening voxels, the track density will depend on a number of factors specific to the pathway, such as the length and dispersion in space. The difference in track density at the ends and middle of a pathway can also be seen in the “U” shape of the track density plotted against position in the single-fiber phantom (Fig. 4(a)). The track density at the middle of the pathway is especially low in Fig. 4(a) because the entire imaging volume is used as the mask, providing a large volume for tracks to disperse. If, at the other extreme, the mask included only the fiber, the track density in the middle of the pathway would be the same as at the seed and target.

Another limitation of this approach is that there is no apparent way to impose geometric constraints on the tracks. The formalism considers the net number of tracks passing through a voxel, but the geometry of the tracks counted may be unphysical. Impossibly sharp bends and multiple visits to the same voxel are, for example, not forbidden. An adjustment of the solution algorithm could, in principle, impose some local constraints. For example, the continuity equation (2) could be solved by finding values in the immediate neighborhood of the seed (2) and iterating until a solution is found at all other voxels in an approach similar front propagation methods proposed by Parker *et al.* [13]. Constraints could be imposed by imposing a cost on the curvature of the front, thereby preventing implausibly sharp turns. The simplest implementation could, for example, start at the seed and solve for the track densities in voxels neighboring the seed using continuity (2). We could then proceed to the neighbor with highest density, solve for the densities in its neighbors and repeat. As we progress from voxel to voxel, we can enforce

physical constraints such as disallowing high bending angles. Once a stopping criterion is met, such as arrival at the target, we would have an approximation of the track density, similar to a first iteration of the Gauss-Seidel method [20]. As the approach is inherently iterative, there may be an undesirable cost in terms of computational burden.

An uncertainty that requires further investigation is the cause of the difference between the PDE and MC results when tracking the transcallosal (Fig. 11) and long association (Fig. A1) pathways. For the transcallosal pathway, while the MC results show a track density through the pons comparable in magnitude to the track density through the corpus callosum, the PDE results show a stronger connection through the corpus callosum. This difference in the PDE results is not simply due to image thresholding or presentation. While the ratio of track density in the pons to that in the corpus callosum is  $\sim 1$  in the MC result, it is only  $\sim 0.01$  in the PDE result. The cause of the difference is unclear, but we did investigate several possibilities. We made modifications to the MC method to mimic features of the PDE algorithm. To approximate the discretization of the fODF in the PDE method, we effectively smeared the fODF by using a smaller maximum order for spherical harmonics. We eliminated the physical constraints in the MC routine that disallow backtracking (bending angles greater than  $90^\circ$ ), which is allowed in the PDE method. We ran the

MC method with these changes separately and together, but saw no decrease in the track density through the pons. The same mask was used for both methods. A similar difference was seen between the PDE and MC results in the superior longitudinal fasciculus. Given that the PDE method was designed to mimic the behavior of the MC method, we are puzzled by the differences seen in Figs. 11 and A1. Further work will examine a wider range of pathways and unravel the reasons driving differences seen between MC and PDE tractography.

## VI. CONCLUSION

We have introduced a generic, probabilistic formalism for tractography that inherently accounts for global information while having a fast implementation. The advantages, particularly with regard to long pathways and pathways along the subcortical surface are demonstrated in simulations and *in vivo*. The results are largely equivalent to a standard Monte Carlo approach, but faster by orders of magnitude. The approach promises to enable whole-brain tractography with little computational burden.

## APPENDIX

We present Figs. A1-A4 referenced in the text.

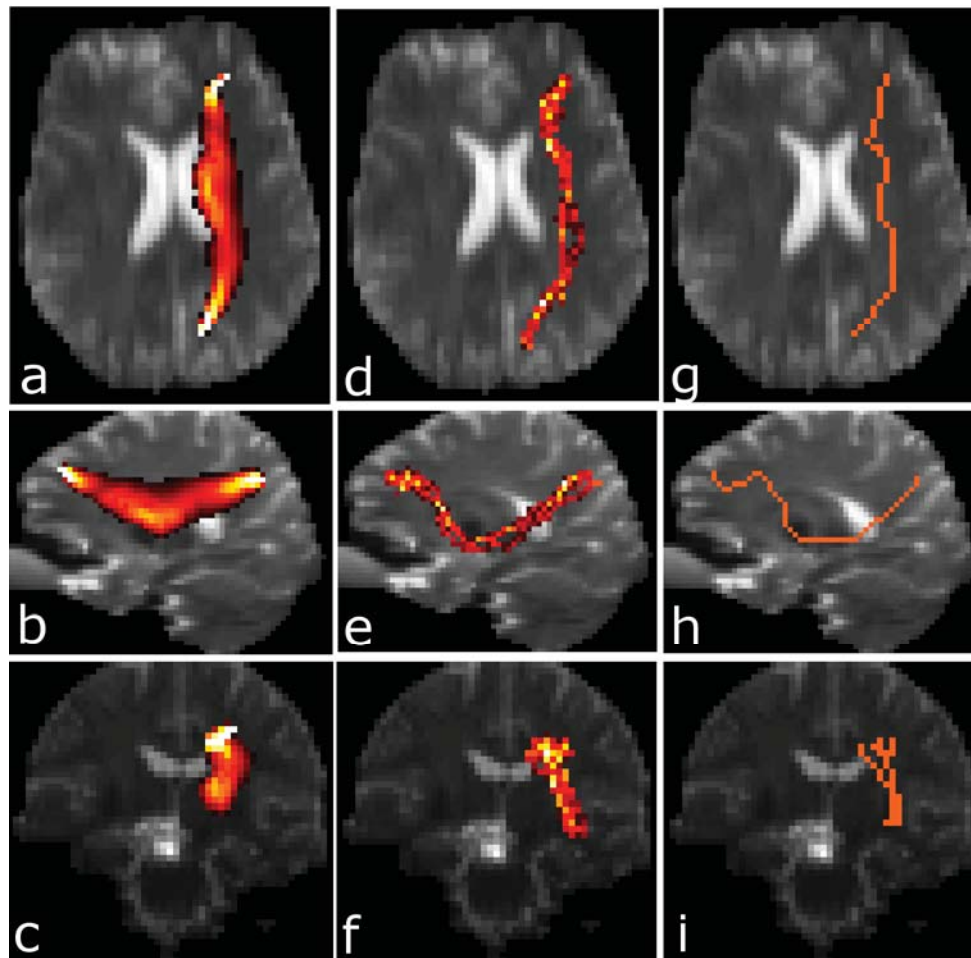


Fig. A1. Maximum intensity projection of the superior longitudinal fasciculus generated by PDE (a-c), Monte Carlo (d-f), and shortest path (g-i) methods. Intensity ranges were set to  $[0.06, 0.25]$  (a-c) and  $[0.01, 1]$  (d-f).



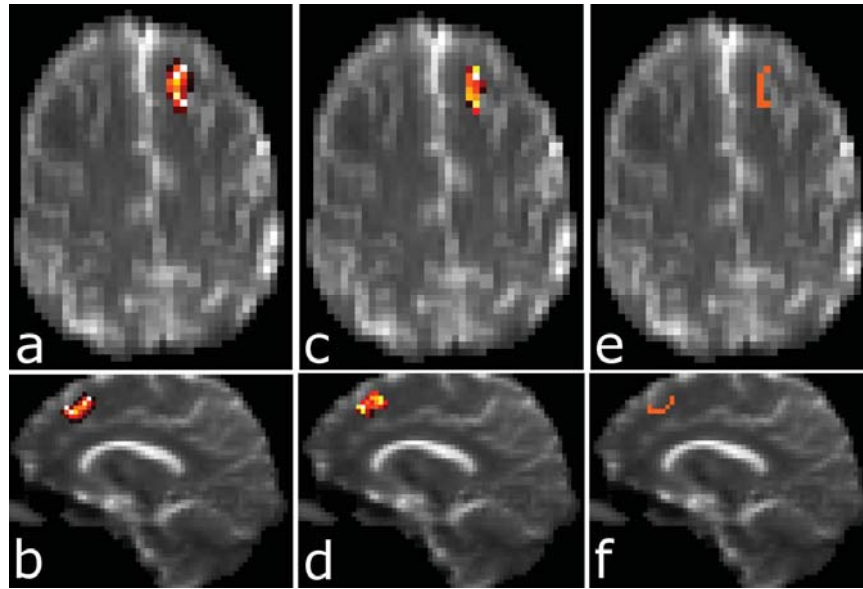


Fig. A2. Maximum intensity projection of a short association fiber (U-fiber) generated by PDE (a, b), Monte Carlo (c, d), and shortest path (e, f) methods. Intensity ranges were set to  $[0.05, 0.5]$  (a, b) and  $[0.4, 1]$  (c, d). Since the length of the fiber is short compared to the voxel resolution, we see that the features of the track are not as distinct as those of longer fibers.

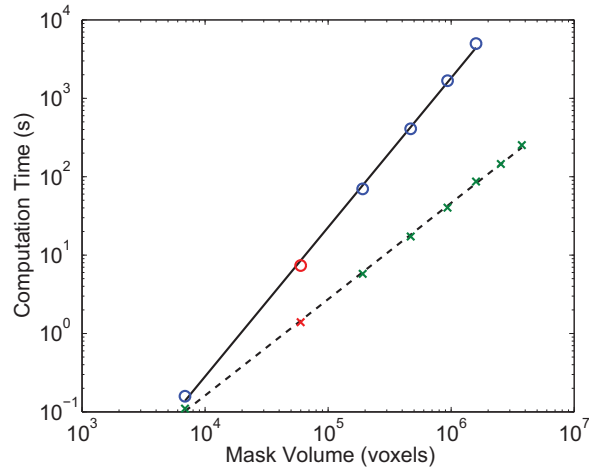


Fig. A3. Log-log plot of PDE (x) and shortest-path (o) computation time vs. number of voxels in the mask. PDE computation time varies linearly with computational volume, while shortest-path time varies quadratically. Linear and quadratic dependence are indicated by the dashed and solid lines, respectively. Red symbols correspond to times for computational volumes approximately equal to that of the *in vivo* data.

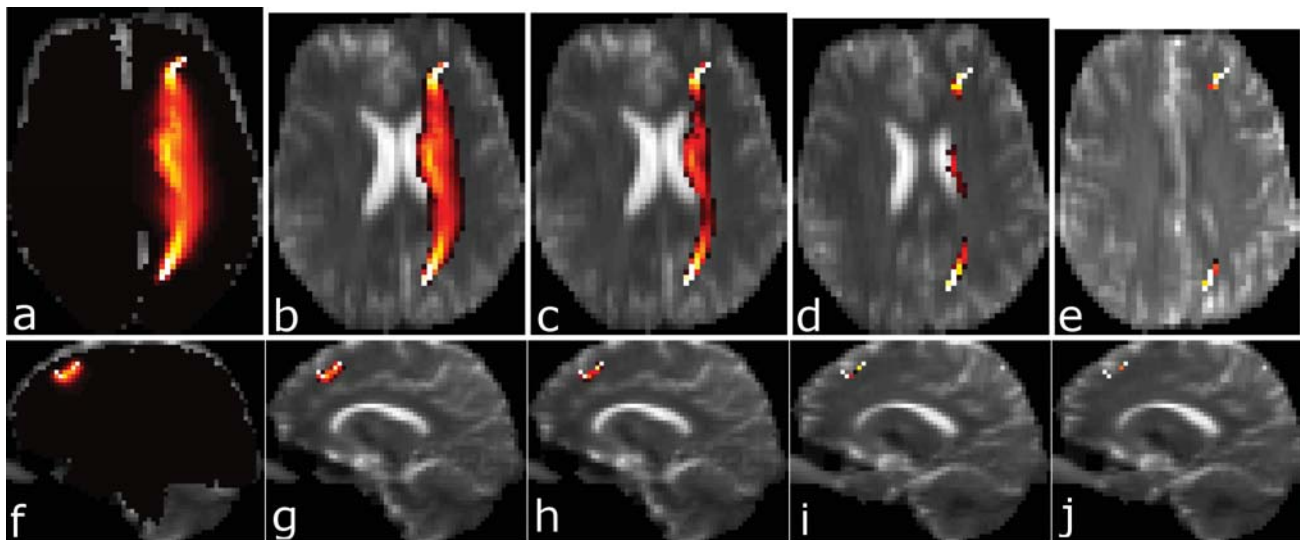


Fig. A4. Comparison of long and short association fibers at different thresholds. (a)-(e) Maximum intensity projections of the superior longitudinal fasciculus at minimum intensity thresholds of 0, 0.05, 0.1, 0.15, and 0.2, respectively. Maximum intensity is set to 0.25 for all five panels. (f)-(j) Maximum intensity projections of a short U-fiber at thresholds of 0, 0.1, 0.2, 0.3, and 0.4, respectively. Maximum intensity is set to 0.5 for all five panels.

## ACKNOWLEDGMENT

We thank Dr. Iturria-Medina of the Cuban Neuroscience Center for sharing his code and expertise. We also thank the reviewers for their helpful criticism and suggestions, the wording of which was partly incorporated in this manuscript.

## REFERENCES

- [1] P. J. Basser, S. Pajevic, C. Pierpaoli, J. Duda, and A. Aldroubi, "In vivo fiber tractography using DT-MRI data," *Magn Reson Med*, vol. 44, pp. 625-32, Oct 2000.
- [2] M. Catani, R. J. Howard, S. Pajevic, and D. K. Jones, "Virtual in vivo interactive dissection of white matter fasciculi in the human brain," *Neuroimage*, vol. 17, pp. 77-94, Sep 2002.
- [3] T. E. Conturo, N. F. Lori, T. S. Cull, E. Akbudak, A. Z. Snyder, J. S. Shimony, R. C. McKinstry, H. Burton, and M. E. Raichle, "Tracking neuronal fiber pathways in the living human brain," *Proc Natl Acad Sci U S A*, vol. 96, pp. 10422-7, Aug 31 1999.
- [4] S. Mori, B. J. Crain, V. P. Chacko, and P. C. van Zijl, "Three-dimensional tracking of axonal projections in the brain by magnetic resonance imaging," *Ann Neurol*, vol. 45, pp. 265-9, Feb 1999.
- [5] T. E. Behrens, H. J. Berg, S. Jbabdi, M. F. Rushworth, and M. W. Woolrich, "Probabilistic diffusion tractography with multiple fibre orientations: What can we gain?," *Neuroimage*, vol. 34, pp. 144-55, Jan 1 2007.
- [6] M. Descoteaux, R. Deriche, T. R. Knosche, and A. Anwander, "Deterministic and probabilistic tractography based on complex fibre orientation distributions," *IEEE Trans Med Imaging*, vol. 28, pp. 269-86, Feb 2009.
- [7] M. J. Lowe, E. B. Beall, K. E. Sakaie, K. A. Koenig, L. Stone, R. A. Marrie, and M. D. Phillips, "Resting state sensorimotor functional connectivity in multiple sclerosis inversely correlates with transcallosal motor pathway transverse diffusivity," *Hum Brain Mapp*, vol. 29, pp. 818-27, Jul 2008.
- [8] T. E. Behrens, M. W. Woolrich, M. Jenkinson, H. Johansen-Berg, R. G. Nunes, S. Clare, P. M. Matthews, J. M. Brady, and S. M. Smith, "Characterization and propagation of uncertainty in diffusion-weighted MR imaging," *Magn Reson Med*, vol. 50, pp. 1077-88, Nov 2003.
- [9] G. J. Parker, H. A. Haroon, and C. A. Wheeler-Kingshott, "A framework for a streamline-based probabilistic index of connectivity (PICO) using a structural interpretation of MRI diffusion measurements," *J Magn Reson Imaging*, vol. 18, pp. 242-54, Aug 2003.
- [10] Y. Iturria-Medina, E. J. Canales-Rodriguez, L. Melie-Garcia, P. A. Valdes-Hernandez, E. Martinez-Montes, Y. Aleman-Gomez, and J. M. Sanchez-Bornot, "Characterizing brain anatomical connections using diffusion weighted MRI and graph theory," *Neuroimage*, vol. 36, pp. 645-60, Jul 1 2007.
- [11] A. Zalesky, "DT-MRI fiber tracking: a shortest paths approach," *IEEE Trans Med Imaging*, vol. 27, pp. 1458-71, Oct 2008.
- [12] N. S. Hageman, A. W. Toga, K. L. Narr, and D. W. Shattuck, "A diffusion tensor imaging tractography algorithm based on Navier-Stokes fluid mechanics," *IEEE Trans Med Imaging*, vol. 28, pp. 348-60, Mar 2009.
- [13] G. J. Parker, K. E. Stephan, G. J. Barker, J. B. Rowe, D. G. MacManus, C. A. Wheeler-Kingshott, O. Ciccarelli, R. E. Passingham, R. L. Spinks, R. N. Lemon, and R. Turner, "Initial demonstration of in vivo tracing of axonal projections in the macaque brain and comparison with the human brain using diffusion tensor imaging and fast marching tractography," *Neuroimage*, vol. 15, pp. 797-809, Apr 2002.
- [14] O. Friman, G. Farneback, and C. F. Westin, "A Bayesian approach for stochastic white matter tractography," *IEEE Trans Med Imaging*, vol. 25, pp. 965-78, Aug 2006.
- [15] E. T. Jaynes, *Probability Theory: The Logic of Science*. Cambridge: Cambridge University Press, 2003.
- [16] J. D. Tournier, F. Calamante, D. G. Gadian, and A. Connelly, "Direct estimation of the fiber orientation density function from diffusion-weighted MRI data using spherical deconvolution," *Neuroimage*, vol. 23, pp. 1176-85, Nov 2004.
- [17] I. Aganj, C. Lenglet, G. Sapiro, E. Yacoub, K. Ugurbil, and N. Harel, "Reconstruction of the orientation distribution function in single- and multiple-shell q-ball imaging within constant solid angle," *Magn Reson Med*, vol. 64, pp. 554-66, Aug 2010.
- [18] D. S. Tuch, "Q-ball imaging," *Magn Reson Med*, vol. 52, pp. 1358-72, Dec 2004.
- [19] V. J. Wedeen, R. P. Wang, J. D. Schmahmann, T. Benner, W. Y. Tseng, G. Dai, D. N. Pandya, P. Hagmann, H. D'Arceuil, and A. J. de Crespigny, "Diffusion spectrum magnetic resonance imaging (DSI) tractography of crossing fibers," *Neuroimage*, vol. 41, pp. 1267-77, Jul 15 2008.
- [20] W. Press, S. Teukolsky, W. Vetterling, and B. Flannery, *Numerical Recipes: The Art of Scientific Computing*, 3rd ed.: Cambridge University Press, 2007.
- [21] P. A. Cook, M. Symms, P. A. Boulby, and D. C. Alexander, "Optimal acquisition orders of diffusion-weighted MRI measurements," *J Magn Reson Imaging*, vol. 25, pp. 1051-8, May 2007.
- [22] K. E. Sakaie and M. J. Lowe, "Quantitative assessment of motion correction for high angular resolution diffusion imaging," *Magnetic Resonance Imaging*, vol. 28, pp. 290-296, Feb 2010.
- [23] A. Leemans and D. K. Jones, "The B-matrix must be rotated when correcting for subject motion in DTI data," *Magn Reson Med*, vol. 61, pp. 1336-49, Jun 2009.
- [24] B. Fischl, A. van der Kouwe, C. Destrieux, E. Halgren, F. Segonne, D. H. Salat, E. Busa, L. J. Seidman, J. Goldstein, D. Kennedy, V. Caviness, N. Makris, B. Rosen, and A. M. Dale, "Automatically parcellating the human cerebral cortex," *Cereb Cortex*, vol. 14, pp. 11-22, Jan 2004.
- [25] J. Ashburner and K. Friston, "Multimodal image coregistration and partitioning--a unified framework," *Neuroimage*, vol. 6, pp. 209-17, Oct 1997.
- [26] K. E. Sakaie and M. J. Lowe, "An objective method for regularization of fiber orientation distributions derived from diffusion-weighted MRI," *Neuroimage*, vol. 34, pp. 169-176, Jan 1 2007.
- [27] D. C. Alexander, G. J. Barker, and S. R. Arridge, "Detection and modeling of non-Gaussian apparent diffusion coefficient profiles in human brain data," *Magn Reson Med*, vol. 48, pp. 331-40, Aug 2002.
- [28] P. Hagmann, J. P. Thiran, L. Jonasson, P. Vandergheynst, S. Clarke, P. Maeder, and R. Meuli, "DTI mapping of human brain connectivity: statistical fibre tracking and virtual dissection," *Neuroimage*, vol. 19, pp. 545-54, Jul 2003.
- [29] B. W. Kreher, I. Mader, and V. G. Kiselev, "Gibbs tracking: a novel approach for the reconstruction of neuronal pathways," *Magn Reson Med*, vol. 60, pp. 953-63, Oct 2008.
- [30] M. Reisert, I. Mader, C. Anastasopoulos, M. Weigel, S. Schnell, and V. Kiselev, "Global fiber reconstruction becomes practical," *Neuroimage*, vol. 54, pp. 955-62, Jan 15 2011.
- [31] V. Arsigny, P. Fillard, X. Pennec, and N. Ayache, "Fast and simple calculus on tensors in the log-Euclidean framework," *Med Image Comput Assist Interv*, vol. 8, pp. 115-22, 2005.
- [32] P. Fillard, X. Pennec, V. Arsigny, and N. Ayache, "Clinical DT-MRI estimation, smoothing, and fiber tracking with log-Euclidean metrics," *IEEE Trans Med Imaging*, vol. 26, pp. 1472-82, Nov 2007.
- [33] X. Hao, R. T. Whitaker, and P. T. Fletcher, "Adaptive Riemannian metrics for improved geodesic tracking of white matter," *Inf Process Med Imaging*, vol. 22, pp. 13-24, 2011.
- [34] S. M. Smith, M. Jenkinson, M. W. Woolrich, C. F. Beckmann, T. E. Behrens, H. Johansen-Berg, P. R. Bannister, M. De Luca, I. Drobnjak, D. E. Flitney, R. K. Niazy, J. Saunders, J. Vickers, Y. Zhang, N. De Stefano, J. M. Brady, and P. M. Matthews, "Advances in functional and structural MR image analysis and implementation as FSL," *Neuroimage*, vol. 23 Suppl 1, pp. S208-19, 2004.

# Correlation of imaging connectivity with electrophysiological connectivity using intracranial electrodes

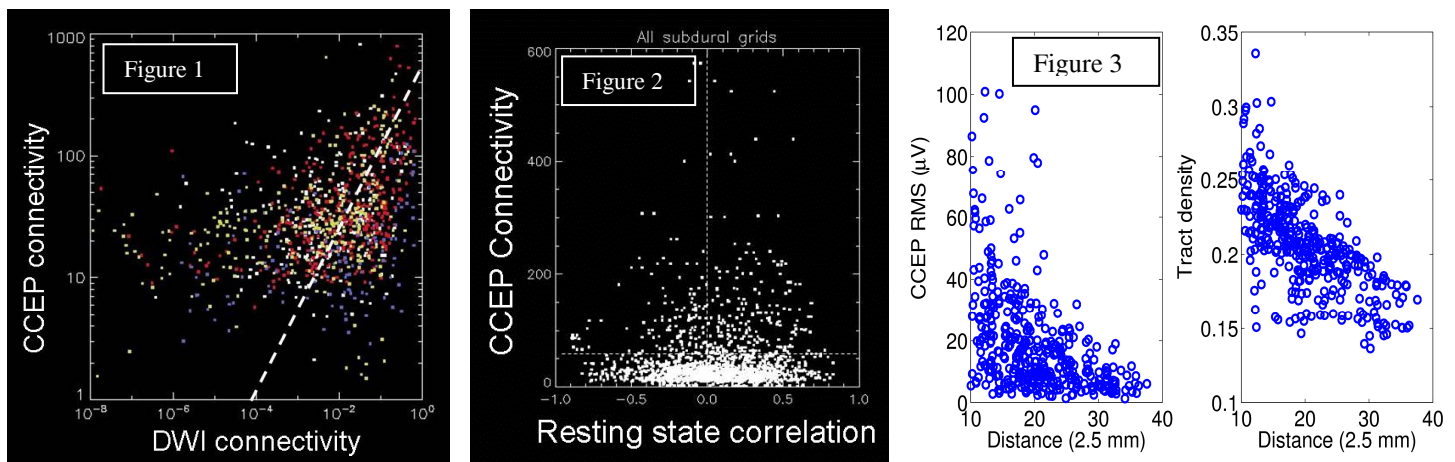
Stephen Jones<sup>1</sup>, Erik Beall<sup>1</sup>, Jorge Gonzalez-Martinez<sup>1</sup>, Blessy Mathew<sup>1</sup>, Dileep Nair<sup>1</sup>, Imad Najm<sup>1</sup>, Michael Phillips<sup>1</sup>, Ken Sakaie<sup>1</sup>, and Myron Zhang<sup>1</sup>  
<sup>1</sup>Cleveland Clinic Foundation, Cleveland, OH, United States

**Target audience:** Diffusion MRI, tractography, intracranial electrodes/EEG, epilepsy

**Purpose:** Diffusion weighted imaging (DWI) can non-invasively infer neural tractography and connectivity, which can reasonably delineate major known pathways. Regarding accuracy, there is continued interest in how well DWI measures of imaging connectivity (IC) correlate with electrophysiological connectivity (EC)—a question of clinical relevance. One standard for measuring EC is cortico-cortical evoked potentials (CCEPs), which uses intracranial electrodes to stimulate and record electrical activity<sup>1</sup>. Here, we compare IC and EC between pairs of regions in the brain varying in space. Although significant correlation between these two measures has been reported<sup>2</sup>, our results indicate that the relation between IC and EC is modest and still uncertain.

**Methods:** CCEP data was obtained in epilepsy patients from both surgically implanted deep stereotactic electroencephalography (SEEG) electrodes, and subdural grid electrodes. EC was evaluated by directly stimulating an electrode contact pair and recording voltage at all other contacts. A measure of EC between contacts X and Y was taken to be the root mean square (RMS) of the recordings at Y, from 10 to 20 ms after X was stimulated.

Prior to implantation, the patient underwent pre-procedural imaging at 3T (2.5mm voxels), which included 61 direction diffusion imaging (HARDI)<sup>3</sup>, and resting-state connectivity. All electrode positions were coregistered to anatomic imaging. We have developed a fast probabilistic tracking method<sup>4</sup>, which was used to compute pathways from each stimulus contact to every other contact, to parallel the CCEPs stimulus. Various IC measures include either mean tract density along pathways, mean tract FA or TD, or mean component along FOD. Data has been obtained from four patients so far.



**Results:** Fig. 1 shows a scatter plot (log-log) of the relation of EC and IC (DWI connectivity) for over 600 contacts in 4 patients; each data point represents a pair of points in the brain. Although there is a significant correlation, there are many points showing high IC with low EC, and visa versa. Fig. 2 shows a similar scatter plot comparing EC with resting-state connectivity, which shows only a mild correlation of EC with IC. Fig. 3 shows a significant distance effect whereby both IC and EC diminish with distance, an effect that further confounds the direct correlation of EC with IC.

**Discussion:** Today, IC is extensively used to study the brain, but there is little evidence supporting various measures of IC. We attempt to derive a measure of IC by comparing values against the presumed gold-standard of EC. We find only a modest correlation with DWI and a minimal correlation with rsMRI. Many pairs of points in the brain have high IC and low EC, or have low IC with high EC. We have explored many variations of both EC and IC measures, and this trend is always observed. Possible causes include incompatibly low MRI resolution, distance effects of both IC and EC, poor co-localization of MRI voxels with electrical contact points, or intrinsic brain functionality whereby a solid structural path between two points does not necessarily imply a strong concordant electrophysiological response. Our results lead us to believe that the connection between EC and IC is tentative. This discordance could be inherent to brain physiology, or it could indicate that our current methodology is not fully understood.

**Conclusion:** An extensive comparison of diffusion MRI and electrophysiological data indicates an uncertain correlation between these two measures of brain connectivity.

<sup>1</sup> Matsumoto, R., et al. (2004). Functional connectivity in the human language system: a cortico-cortical evoked potential study. *Brain*, 127(10), 2316-2330.

<sup>2</sup> Conner, C. R., et al. (2011). Anatomic and electro-physiologic connectivity of language A combined DTI-CCEP study. *Computers in bio and med*, 41(12), 1100-1109.

<sup>3</sup> Tuch, D. S., et al. (2002). HARDI reveals intravoxel white matter fiber heterogeneity. *Magnetic Resonance in Medicine*, 48(4), 577-582.

<sup>4</sup> Zhang, M., Sakaie, K. E., & Jones, S. E. (2012). Toward whole-brain maps of neural connections: Logical framework and fast implementation. *MMBIA 2012 Proc.* (pp. 193-197). IEEE.